


Article

A Novel Wireless-Netted UWB Life-Detection Radar System for Quasi-Static Person Sensing

Kun Yan ^{1,2,3} , Shiyou Wu ^{1,2,*}, Shengbo Ye ^{1,2} and Guangyou Fang ^{1,2}

¹ Aerospace Information Research Institute, Chinese Academy of Sciences, No. 9 Dengzhuang South Road, Haidian District, Beijing 100094, China; yorkstudio@foxmail.com (K.Y.); shengboye@163.com (S.Y.); gyfang@mail.ie.ac.cn (G.F.)

² The Key Laboratory of Electromagnetic Radiation and Sensing Technology, Chinese Academy of Science, Haidian District North 4th Ring West Road 19th, Beijing 100190, China

³ School of Electronic, Electrical and Communication Engineering, University of the Chinese Academy of Sciences, Beijing 100039, China

* Correspondence: wusy@aircas.ac.cn

Abstract: In actual life-detection radar applications, a quasi-static person with weak respiration is difficult to find when relying on the echoes from a single fixed observation point. To effectively sense the weak respiration of a quasi-static person in complex through-wall and through-floor conditions, this paper proposes a novel multi-observation point detection system composed of multiple Golay complementary coded radars in which communication and synchronization are carried out wirelessly. The collaboration structure and Golay complementary coded transmitter improve the signal to noise ratio (SNR). Proof-of-principle experiments are carried out with our designed radar prototype and prove that the radar system can detect a respiring target 21 m behind a brick wall or a respiring target behind two levels of reinforced concrete floors, validating the effectiveness of a multi-observation point working mode for the efficient detection of weak human respiration.

Keywords: life detection radar; multi-observation point system; through-the-wall radar; Golay complementary code



Citation: Yan, K.; Wu, S.; Ye, S.; Fang, G. A Novel Wireless-Netted UWB Life-Detection Radar System for Quasi-Static Person Sensing. *Appl. Sci.* **2021**, *11*, 424. <https://doi.org/10.3390/app11010424>

Received: 9 December 2020

Accepted: 30 December 2020

Published: 4 January 2021

Publisher's Note: MDPI stays neutral with regard to jurisdictional claims in published maps and institutional affiliations.



Copyright: © 2021 by the authors. Licensee MDPI, Basel, Switzerland. This article is an open access article distributed under the terms and conditions of the Creative Commons Attribution (CC BY) license (<https://creativecommons.org/licenses/by/4.0/>).

1. Introduction

In rescue applications, there is increasing demand for mechanisms to improve the capability to sense trapped persons in complex scenes. Ultra-wideband (UWB) radar technology provides strong anti-interference ability, high-range resolution and penetrability, which plays an important role in detecting trapped persons [1–4]. It can detect the vital signs of trapped quasi-static persons with weak micro-movements [5–8]. However, the detection capability of single fixed observation point systems is limited in complex conditions. In order to increase the detection capabilities and detection rate of weak respiration targets in complex environments, novel transmit signal designs are proposed for higher signal to noise ratios (SNRs) in [9–13]. The multiple input–multiple output (MIMO) technology, which uses a real aperture with multiple transceiver combinations, presents an instant imaging resolution and high clutter suppression capability, and it has been widely used in [14–18]. Further, the multi-view and netted radar systems were found to improve the SNR and increase rescue efficiency in [19–22]. The development of UWB radar vital sign detection techniques that allow multi-point observation and data association processing is becoming a priority, motivating the design of multi-observation point detection systems that increase rescue efficiency.

In this paper, we propose a novel multi-observation point detection system composed of multiple Golay complementary coded UWB life-detection radars. The communication and synchronization between radars are carried out wirelessly. For the echoes received at different observation points, to improve the SNR of vital signs, the cross-correlation

operation is performed in the slow-time dimension. Meanwhile, the use of a low sidelobe sinusoidal modulation Golay complementary coded signal with a center frequency of about 1 GHz as the transmit signal can further improve the SNR. In addition, the self-positioning technology is deployed in each UWB life-detection radar to make their positions known. Finally, three experiments are carried out involving penetrating walls and reinforced concrete floors, verifying the detection performance of the proposed multi-observation point detection system.

2. Multi-Observation Point Detection System

As shown in Figure 1, the architecture of the proposed wireless-netted multi-observation point detection system includes several independent single-channel Golay complementary coded UWB life-detection radars, which are taken as the network nodes controlled by a control host. The radars are responsible for the generation, transmission and reception of the Golay complementary coded signal. The detailed design of the system is discussed in Section 3. The control host is responsible for the human-machine interface, collaborative acquisition and data processing. By using time division multiplexing (TDM) and the star topology, the control host coordinates these network nodes during the multiple observation point detection process to prevent mutual interference.

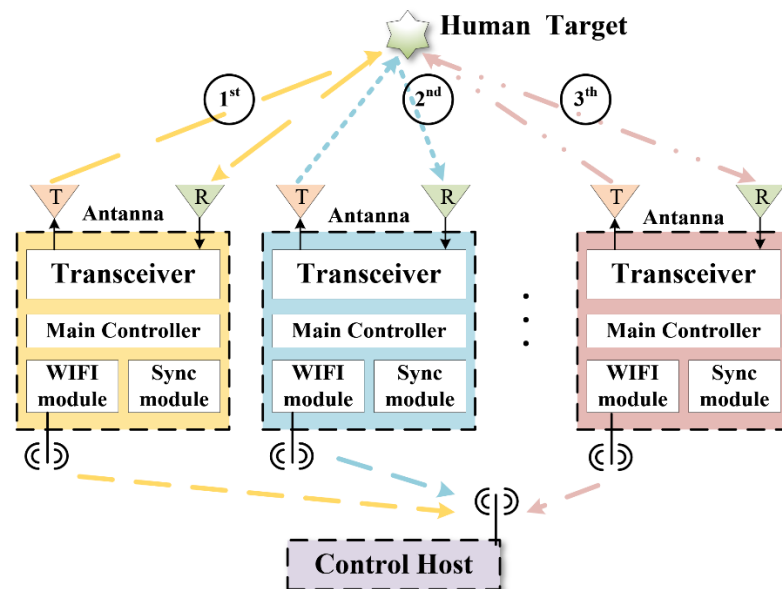


Figure 1. The wireless-netted multi-observation point detection architecture.

3. Design of Golay Complementary Coded Radar

The block diagram of the Golay complementary coded radar for a multi-observation point detection system is shown in Figure 2. There are six key components: a digital transmitter, a dual-channel receiver, a clock manager, a network clock, a self-positioning module and a wireless communication module. A Xilinx Artix-7 Field Programmable Gate Array (FPGA) is used as the main controller unit to manage the peripherals of the radar. To reduce the system cost and improve the spurious-free dynamic range, the equivalent-time sampling technique is adopted. A 16-bit analog to digital converter (ADC) with a maximal sampling rate of 160 Mbps and a full power bandwidth of 1.4 GHz is used as the receiver. A pair of bow-tie antennas are used for electromagnetic radiation and reception. A W5300 chip is used to exchange the raw radar data and commands with the control host by the TCP network protocol, and the wireless bridge realizes the wireless communication. In the following, the Golay complementary coded signal transmitter (marked A in Figure 2), the network clock module (marked D in Figure 2), the self-positioning module (marked E in Figure 2) and antennas are described in detail.

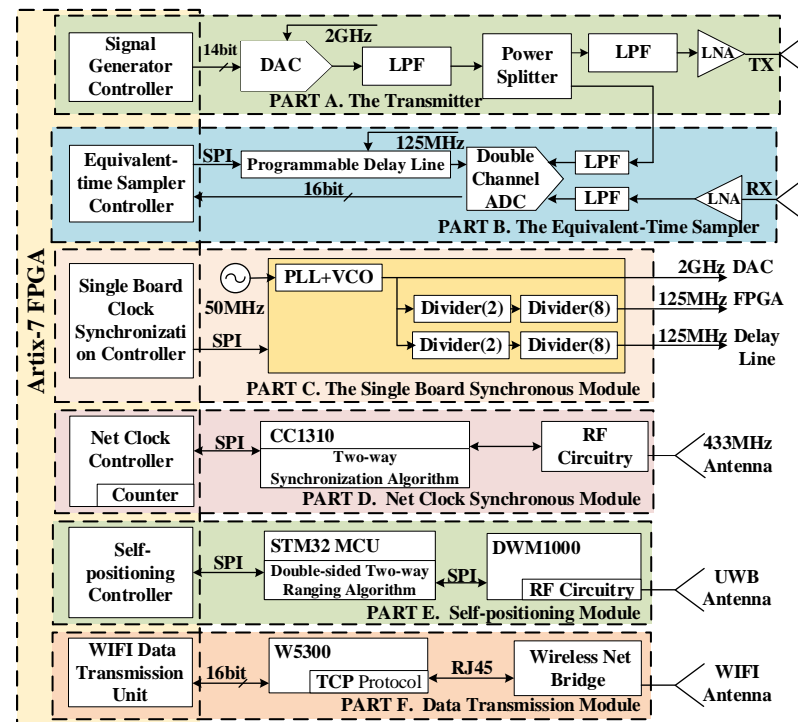


Figure 2. The block diagram of the Golay complementary coded radar. UWB: ultra-wideband.

3.1. The Golay Complementary Coded Signal Transmitter

The selection of the transmitting signal is a key element of the radar system. The pseudo-random sequence has been widely applied to modulate the transmitting signal of through-the-wall radar due to its high signal to noise ratio (SNR) and high range resolution [23,24]. Of these, the m-sequence, Gold sequence and Golay complementary sequence are most commonly used. The m-sequence has long been applied to UWB radars due to its good autocorrelation characteristics. However, the number of m-sequences is small, so alternative sequences of a fixed-length are limited. The Gold sequence is based on the m-sequence and has low autocorrelation but better cross-correlation than the m-sequence. There are a greater number of sequences, which can be used for multiple input–multiple output (MIMO) radars. The Golay complementary sequence contains two sub-codes; the autocorrelation functions of the two sub-codes can be added together to eliminate the side-lobes. The peak side-lobe ratio is better than that of the m-sequence, but the Golay complementary sequence’s time efficiency is low.

Determining trapped human beings from raw radar echoes is extremely difficult due to micro-motion and the low reflectivity of the human body. The autocorrelation characteristic is the essential reference standard for selecting the pseudo random code. In combination with our previous research work [25], setting the Golay complementary coded signal as the transmitting signal can avoid the weak reflection target’s echo signal being submerged by the side-lobes due to its high peak side-lobe ratio, thus further improving the penetration capability and anti-noise capability of the radar.

Consider a binary sequence $\mathbf{a} = [a_0, a_1, \dots, a_{N-1}]^T$, where N means the length of sequence \mathbf{a} ; its aperiodic autocorrelation is defined as

$$C_{a,a}(k) = \sum_{j=0}^{N-1-k} a(j)a(j+k), 0 \leq k \leq N-1. \quad (1)$$

Consider two sequences with the length of N : $\mathbf{a} = [a_0, a_1, \dots, a_{N-1}]^T$ and $\mathbf{b} = [b_0, b_1, \dots, b_{N-1}]^T$, $a_i, b_i \in \{1, 0\}$. If \mathbf{a} and \mathbf{b} satisfy the requirement of (2), they can be called a Golay complementary pair.

$$C_{a,a}(k) + C_{b,b}(k) = \begin{cases} 2N, k = 0 \\ 0, k \neq 0 \end{cases} \quad (2)$$

The Golay complementary pair has good autocorrelation characteristics with no side-lobes, and the signal peak is doubled. Any sequence included in a Golay complementary pair is called a Golay complementary sequence [26]. The signal modulated by sequence \mathbf{a} can be called Golay coded signal A, while the signal modulated by sequence \mathbf{b} can be called Golay coded signal B. In our proposed system, a single radar only has one transceiver channel for electromagnetic detection; the radar uses Golay coded signal A, and Golay coded signal B executes electromagnetic detection in turn, and their aperiodic autocorrelation sum forms the radar A-scan. It should be noted that the high autocorrelation characteristic of the Golay complementary sequence comes at the expense of time efficiency, which causes a lower scan rate of the radar system than other pseudo random sequences. Due to the division of time slices in the TDM netted radar system, a single radar's scanning rate is further reduced, which causes limited detectability for high-frequency movements. The balance between the number of observation points and radar scan rate should be considered during system design. In practical terms, the netted radar system scan rate proposed in the article is about 32 fps (see Section 4), which can detect human breathing effectively.

As shown in Figure 2a, the Golay complementary coded signal transmitter consists of a controller in FPGA, a 14-bit digital to analog converter (DAC) at a 2.5 GSPS update rate, two low-pass filters, a power divider and a low-noise amplifier with 21 dB gain. In order to adequately utilize the bandwidth of the antenna and emit more energy, the Golay complementary sequence is modulated by a sinusoidal signal. Meanwhile, to balance the penetration ability and the miniaturization of the antenna [27], the Golay complementary sequence with ~ 1 ns impulse width and a center frequency of ~ 1 GHz is adopted here.

For the modulation of the Golay complementary coded signal, the value "1" in the sequence represents a single positive impulse, while the value "0" represents a single negative impulse. Instead of storing the transmitted waveform directly, both the single positive impulse and the single negative impulse are stored by bit. In this way, fewer ROMs of FPGA are required. A power divider divides the filtered Golay complementary coded signal into two identical signals: one is fed to the transmitting antenna for radiation, while the other is fed to the first channel of the receiver to obtain the reference signal for the pulse compression. The transmitted signal is shown in Figure 3a. In Figure 3b, the autocorrelation results of the Golay complementary coded signal A and signal B are presented, and the sidelobe of the sum of both is under -40 dB.

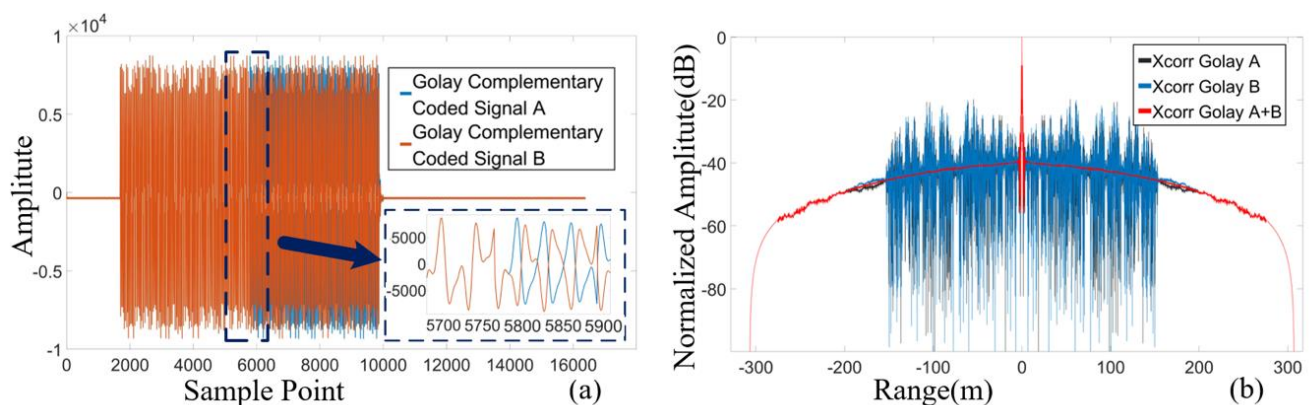


Figure 3. (a) The Golay complementary coded signal sampled by the receiver. (b) The autocorrelation result of Golay code A, Golay code B and the sum of both.

3.2. The Network Clock Module

During the multiple observation point detection process, the accurate network clock module is required to avoid mutual interference between radars which need to be activated in their own time-slices; that is, by setting a time margin and executing wireless clock synchronization, the mutual interference between radars can be prevented effectively. Here, as shown in Figure 2d, the network clock module is designed to include a SimpleLink Sub-1 GHz module based on Texas Instruments' CC1310 chip, a counter and a network clock controller in FPGA. A counter in FPGA begins to count at an interval of 1 microsecond after power-on and plays the role of the local network clock for each radar. For different radars, the corresponding counter (called the network clock) has a different initial offset and clock drift. Assuming that the counter's value of the first radar joining the network is m_1 , the counters' values of the remaining radars can be expressed as $m_n = m_1 + S_n + T_n$, where n means the radar IDs, S_n represents the clock drift and T_n represents the initial offset of non-simultaneous start-up. m_1 is set as the time base for all radars to realize the TDM.

S_n can be expressed as $S_n = p * m_1$, where p represents the frequency tolerance of the radar's main oscillator. For the worst case, a crystal oscillator with ± 10 ppm frequency tolerance might introduce a 20 microsecond error within 1 s. As the human respiration detection algorithm requires 16 s of sampling echoes for one detection, the minimum time margin for S_n is 320 μ s. The measurement process of T_n can be regarded as wireless clock synchronization between radars, and all radars' local network clocks need to be set to m_1 after the synchronization. Here, the CC1310 SimpleLink Sub-1 Ghz module deployed on each radar is used for wireless clock synchronization. The chip provides a set of timers and taggers for radio operation. By sending and receiving the synchronization request twice, the modules can measure the differences of the local network clocks between two radars via a two-way synchronization algorithm [28], where the algorithm is similar to the Network Time Protocol. In order to avoid mutual interference between radars, the CC1310 synchronization module is activated only once for each detection. Therefore, T_n can be measured between the first radar (its local network clock is m_1) and other radars in turn. In addition, the measurement of the CC1310 has an error of ± 10 μ s, which should be added into the time margin. In practical terms, the time margin of the network clock module is set as ~ 15 ms, which is longer than the above requirements (see Section 4). Thus, the clock drift and measurement error would not make the radar network clock invalid.

3.3. The Self-Positioning Module

As the relative positions between radars are needed for human respiration detection, the acquisition of all radars' positions in the architecture of the proposed multiple observation point detection system cannot be neglected. Normally, the relative positions between radars are measured manually in an actual environment, which is not suitable for field applications because of manual measurement errors and the time required. To overcome this problem, a self-positioning module is deployed in each radar to sense its relative position and upload it to the control host automatically.

As shown in Figure 2e, the self-positioning module is composed of a DWM1000 ultra-wideband module, an STM32 Microcontroller Unit (MCU) and a self-positioning controller in FPGA. The DWM1000, as the key component of the self-positioning module, is designed based on Decawave's DW1000 chip. It integrates antenna, all RF circuitry, power management and clock circuitry into one module, supports four radio frequency bands from 3.5 GHz to 6.5 GHz, provides the function of timestamping and precise control of transmission times and can be used in the two-way ranging or Time Difference of Arrival (TDOA) positioning with an error within 10 cm [29–32]. Here, the two-way ranging is realized by the double-sided two-way ranging algorithm executed in the STM32 MCU to achieve the self-positioning of the radars.

Although the workflows of the network clock synchronization module and self-positioning module are similar, it should be noted that the CC1310 and the DWM1000 are not interchangeable; the clock frequency of the CC1310, which serves the timestamp register,

is too low to provide accurate self-positioning, while the configuration and algorithm of the DWM1000 are cumbersome and need to be controlled by an MCU, the random response time of which might cause a network clock synchronization error.

3.4. The Antennas

The size of antennas is essential in radar design. A miniaturized radar is more adaptable to the environment. A certain compromise was made in this work between bandwidth and efficiency when designing the antenna to meet the requirements of using the ultra-wideband and having a miniaturized size. Large bandwidth and high efficiency can be obtained in a smaller size by using a bow-tie antenna. The top-layer patch of the antenna has a semi-elliptical shape, meaning that the current flows through a longer path in a small size. Simultaneously, an elliptical end is added to the bottom layer, coinciding with the top layer. By loading resistors on the bottom side, the current is coupled through the substrate for further absorption, which improves the radiation efficiency of the antenna. The use of a metal back cavity can also enhance the antenna's forward radiation ability while further improving the isolation of the transmitting and receiving antenna and the SNR of the radar system. The size of a single antenna is $140 \text{ mm} \times 70 \text{ mm} \times 35 \text{ mm}$, as Figure 4 shows, and the operating band is 0.5–1.5 GHz.

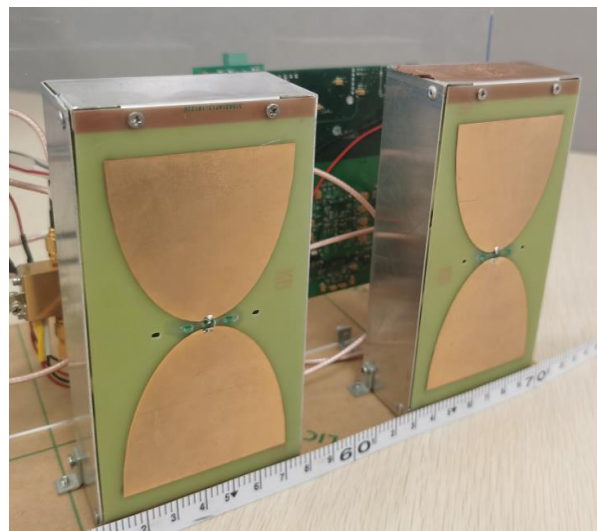


Figure 4. The antennas.

4. Radar Coordination

The orderly collaboration between radars depends on reasonable time-slice management and workflow management; in this work, these were designed in accordance with the radar parameters in Table 1.

Table 1. Key parameters of the proposed radar system. ADC: analog to digital converter.

Property	Proposed Radar
Netted radar system scan rate	32 fps
Center frequency of radar system	1 GHz
Equivalent sampling frequency (F_S)	16 GSPS
Real-time sampling frequency	125 MSPS
Sampling points (N)	16,384
Average times (N_A)	32
ADC Resolution	16 bits

We configured the equivalent-time sampling rate and the real-time sampling rate of the receiver to be 16 GSPS and 125 MSPS, respectively. Accordingly, the receiver was able to

obtain $N = 16,384$ sampling points for one UWB A-scan in 512 μs , equaling 128 pulse repeat periods. To improve the echo's SNR, $N_A = 32$ UWB A-scans were required for human respiration detection, and the corresponding time consumption was about 17 ms. In addition, the wireless data transmission for transmitting the radar echoes and the reference signal for pulse compression with a network speed of 100 Mbps required about 6 ms. Thus, the required minimum time slice was about 23 ms. In practical terms, to retain the time margin for wireless transmission and the network clock module, each time slice was set as 32 ms.

To understand the orderly collaboration between radars, the workflow timing is presented in Figure 5.

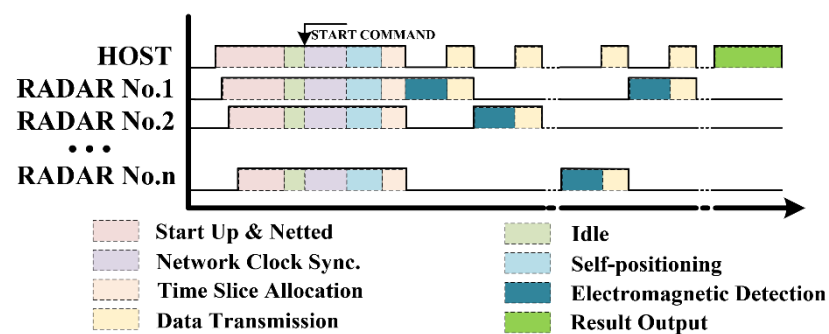


Figure 5. The workflow timing.

- (1) *Start Up and Netted*: As the initialization stage, the host establishes the WIFI network and permits radars access. Radar IDs are distributed by the host for data acquisition, clock synchronization and self-positioning.
- (2) *Idle*: All components turn to the standby mode, waiting for the “start command”.
- (3) *Network Clock Synchronization*: The network clock synchronization is executed firstly after receiving the “start command”.
- (4) *Self-positioning*: The relative positions between radars are measured by their self-positioning modules once.
- (5) *Time Slice Allocation*: The host verifies the validity of the radars’ topology and allocates time slices to radars.
- (6) *Electromagnetic Detection*: According to the network clock synchronization and the time slice allocation, each radar illuminates the target area and receives the echoes within their time slices in turn.
- (7) *Data Transmission*: The echoes are uploaded to the host.
- (8) *Result Output*: After 16 s of sampling echoes, the host calculates the target’s position and displays the results on the human–machine interface.

5. Algorithm Description for Multi-Observation Point Detection System

Denote $S(k, m)$ as the slow-time range matrix obtained at a single observation point, where $k = 0, 1, \dots, K-1$ is the range cell index, and $m = 0, 1, \dots, M-1$ is the slow-time index. For quasi-static trapped human beings with quasi-periodic but weak respiration, we denote $S_i(k, m)$ and $S_j(k, m)$ as the output slow-time range matrixes obtained from the i th and j th ($i \neq j$) observation points after eliminating the time-invariant clutter/interference, respectively. Due to the cross-correlation function of the non-periodic noise being prone to zeroing, the cross-correlation between $S_i(k, m)$ and $S_j(k, m)$ is applied to improve the low signal-to-noise ratio (SNR). However, the quasi-periodic component and its harmonic components contained in the slow-time signal $S_i(k, m)$ and $S_j(k, m)$ are still preserved. Assume that the size of $S_i(k, m)$ and $S_j(k, m)$ are $K_u \times M_a$ and $K_v \times M_b$, respectively. The cross-correlation function $R_{ij}(u, v, m)$ is defined as

$$R_{ij}(u, v, m) = \mathbf{E}\{S_i(k_u, m_a) \cdot S_j(k_v, m_b)\} \quad (3)$$

$$R^{AN}_{ij}(u, v, m) = \max_m \{R_{ij}(u, v, m)\} \cdot \text{AN}_m \{R_{ij}(u, v, m)\} \quad (4)$$

where the range cell index $k_u \in [0, K_u - 1]$ and $k_v \in [0, K_v - 1]$, the slow-time cell index $m_a \in [0, M_a - 1]$, $m_b \in [0, M_b - 1]$ and $m = m_a - m_b$. Then, the advance normalization (AN) method is applied to $R_{ij}(u, v, m)$ so that the weak quasi-periodic component of the quasi-static trapped human being can be further enhanced. We denote the output result of the AN method as $R^{AN}_{ij}(u, v, m)$. The Fourier transform of $R^{AN}_{ij}(u, v, m)$ is taken in each slow-time dimension, and the maximum corresponds to the quasi-static trapped human being; i.e., $(u_{i\max}, v_{j\max})$ indicates the possible range location of the quasi-static trapped human being depending on the different i th and j th observation points.

$$(u_{i\max}, v_{j\max}) = \operatorname{argmax}_{uv} \{\text{FFT}_m \{R^{AN}_{ij}(u, v, m)\}\}, u \neq v \quad (5)$$

6. Experiments and Results

In this section, three types of experimental scenes are designed to simulate complex through-wall conditions. The corresponding experiments were carried out to verify the performance of the proposed multiple observation point detection system. Two layers of brick walls or reinforced concrete floors were penetrated to detect human respiration in type-I (see Figure 6a) and type-II (see Figure 6b) experimental scenes, respectively. For the type-III scene, the propagation distance effect in the through-wall condition is considered. Because of the high radar prototype cost, two Golay complementary coded UWB life-detection radars were used in three experiments. For simplicity, the two radars are labeled as radars No.1 and No.2, respectively. The tested human subject is indicated by the dotted frame in the figure.

As shown in Figure 6a, the type-I experiment was carried out in an apartment unit with various sundry items such as a refrigerator, TV and desktop computer, and the two Golay complementary coded UWB life-detection radars are placed on the same side of the 27 cm brick wall 1.5 m apart. The tested human subject with weak respiration stood at a distance of 4.7 m from radar No.1 and 4.8 m from radar No.2. The type-II experiment was carried out in a building under construction, as shown in Figure 6b. There was electromagnetic interference caused by signal transmission lines and cars. Two radars were placed on the fourth floor 1 m apart. The width of the reinforced concrete floor was 12 cm. The tested human subject lay on the second floor. The distances between him and radars No.1 and No.2 were 6.7 m and 6.8 m, respectively. The type-III experiment was carried out in a stadium, as shown in Figure 6c. An air conditioner and high-power lighting facilities were the main sources of electromagnetic interference. The two radars were placed on the same side of a 37 cm brick wall 2.2 m apart. The tested human subject stood behind the wall, at a distance of 21.6 m from radar No.1 and 21.3 m from radar No.2.



Figure 6. Experimental scenes: (a) type-I scene, (b) type-II scene, (c) type-III scene.

Normally, the echoes from a single radar can be processed by any fast Fourier transform (FFT)-based respiration detection method—for example, the one in [33]—to extract the human breathing frequency. However, due to the low signal to noise ratio (SNR) in these three types of experimental scenes, as shown in Figure 7, all the output range–frequency images are too noisy to distinguish the vital sign features (VSFs). Under the architecture of the proposed multiple observation point detection system, the echoes from the two Golay complementary coded UWB life-detection radars were suitable for association processing to generate the new form of the VSF.

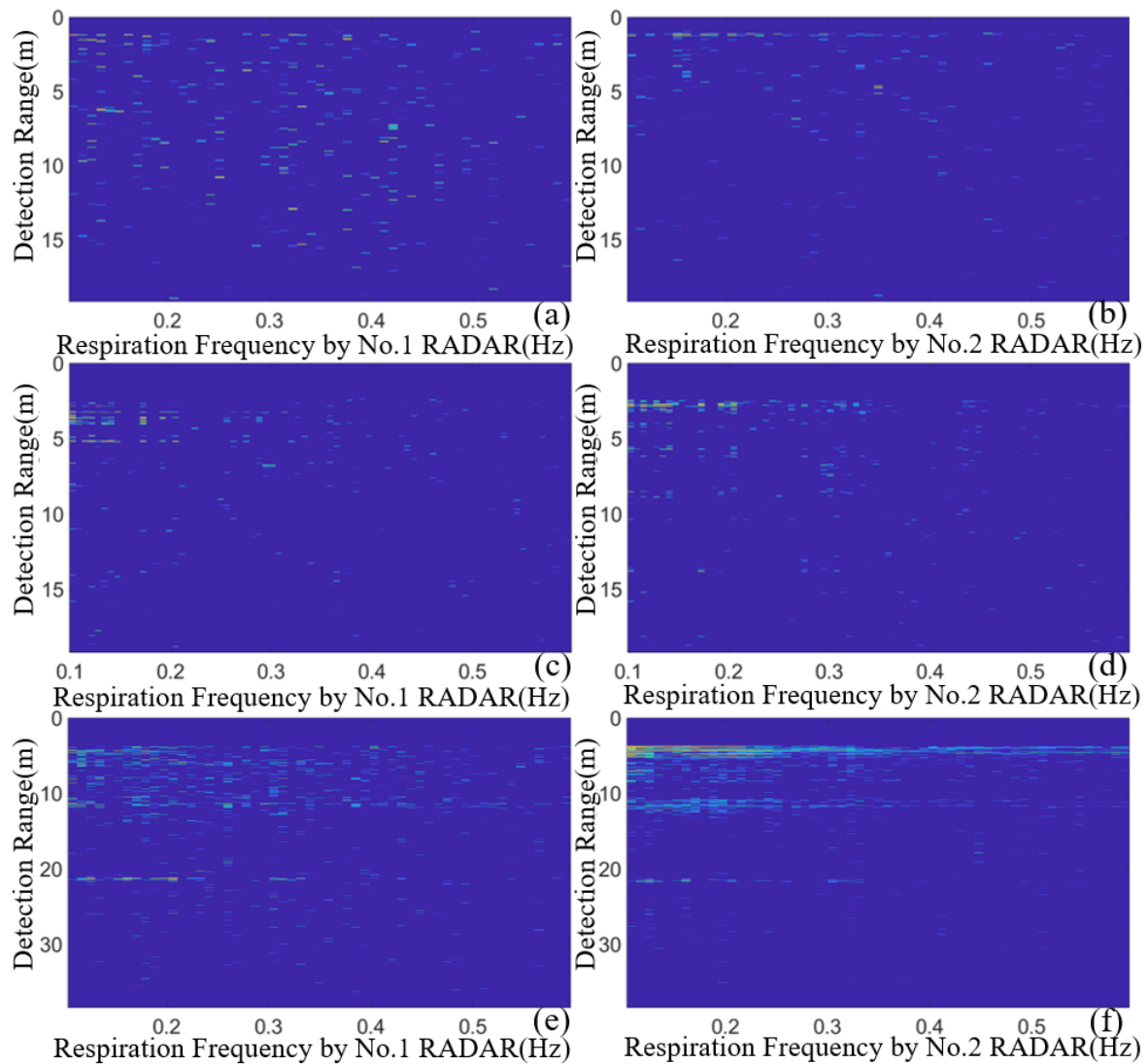


Figure 7. The output range–frequency images using the normal fast Fourier transform (FFT)-based respiration detection methods using the echoes from a single radar. (a,b) Type-I experimental results. (c,d) Type-II experimental results. (e,f) Type-III experimental results.

According to our proposed multi-observation point detection method, when weak respiration movement is present, a new type of VSFs of the tested human subject may appear in the output cross-correlated range–frequency 3D image. The three dimensions of the output cross-correlated range–frequency 3D image represent the range from radar No.1, the range from radar No.2 and the respiration frequency, respectively. As shown in Figure 8a–c, by finding a suitable threshold, the VSFs for the three types of experiments are remarkable. The respiration frequencies indicated by the VSFs are 0.32 Hz, 0.3 Hz and 0.28 Hz, respectively, which are consistent with the actual situation. To further understand the VSFs in the output cross-correlated range–frequency 3D images, 2D slice (range \times range) images corresponding to the specific respiration frequencies of 0.32 Hz, 0.3 Hz and 0.28 Hz are presented in Figure 9a–c, respectively.

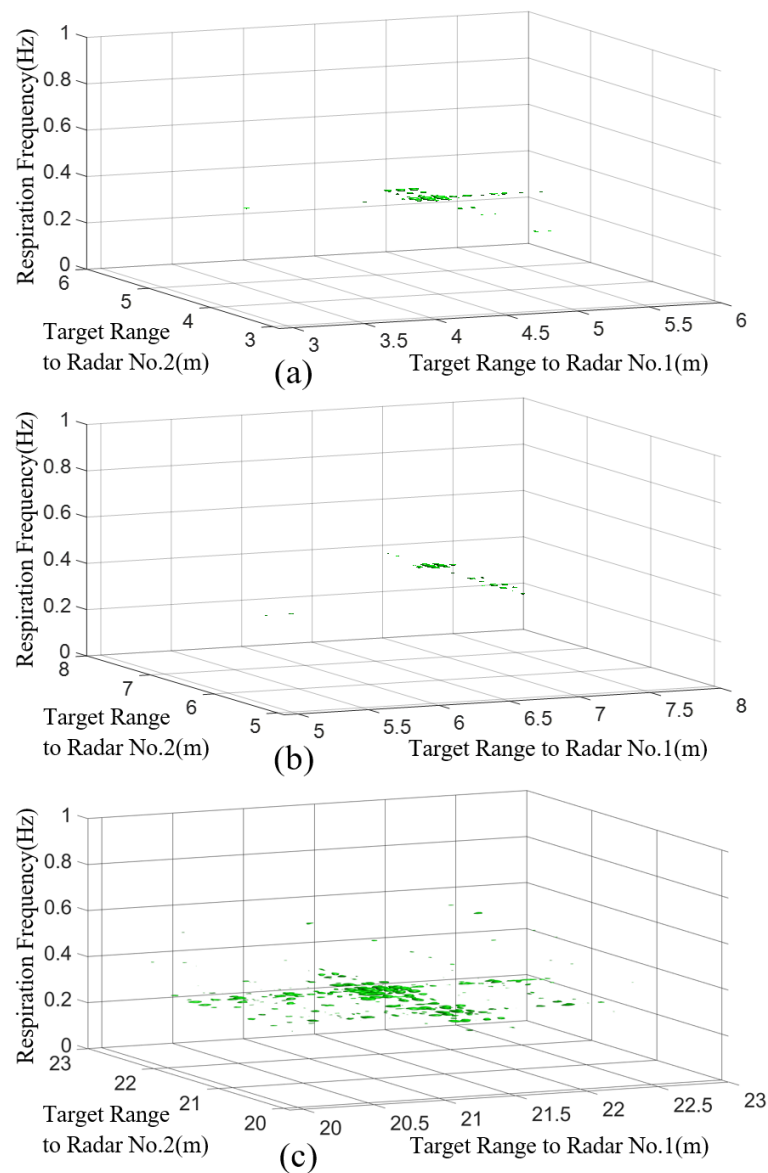


Figure 8. The output cross-correlated range-frequency 3D images. The vital sign features (VSFs) are marked in green for (a) the type-I, (b) the type-II and (c) the type-III experiments, respectively.

Depending on some threshold detectors, the maximum projection for each range dimension can be used to extract the values of distances from radars No.1 and No.2 based on the VSFs.

For the type-I experiment, the distances from radars No.1 and No.2 are 4.72 m and 4.82 m, respectively. For the type-II experiment, the distances from radars No.1 and No.2 are 6.75 m and 6.82 m, respectively. For the type-III experiment, the distances from radars No.1 and No.2 are 21.61 m and 21.28 m, respectively. Thus, the locations of the tested human can be determined by substituting these distances into a “triangulation method”. Note that the locations of the tested human subject in the three types of experiments would be uncertain when using only the echoes from a single radar.

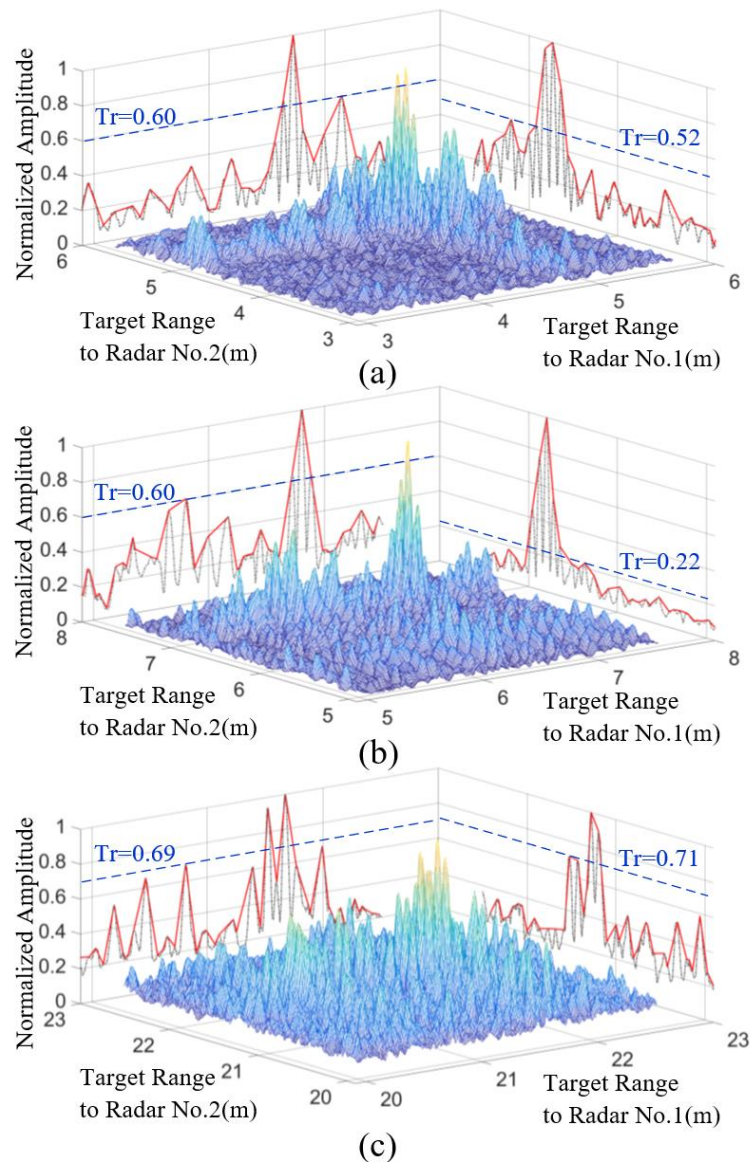


Figure 9. The output 2D slice (range \times range) images for the specific respiration frequencies in (a) the type-I, (b) the type-II and (c) the type-III experiments, respectively.

For the type-I experiment, the distances from radars No.1 and No.2 are 4.72 m and 4.82 m, respectively. For the type-II experiment, the distances from radars No.1 and No.2 are 6.75 m and 6.82 m, respectively. For the type-III experiment, the distances from radars No.1 and No.2 are 21.61 m and 21.28 m, respectively. Thus, the locations of the tested human can be determined by substituting these distances into a “triangulation method”. Note that the locations of the tested human subject in the three types of experiments would be uncertain using only the echoes from a single radar.

7. Conclusions

In this paper, a novel multi-observation point detection system composed of multiple Golay complementary coded UWB life-detection radars is proposed, and its performance in the context of weak human respiration detection is evaluated in complex through-wall conditions. The experiments show that the radar system has excellent detection performance: in the through-the-wall scenario, the radar system could detect a respiring target over 21 m distant, while in the through-the-floor setting, it could detect weak breathing target behind two levels of reinforced concrete floors. Both the design and the coordination of the

Golay complementary coded UWB life-detection radar are illustrated in detail. Remarkably, in the complex through-wall conditions, the weak respiration movement of the tested human subject could be distinguished by the new VSFs that appeared in the output range-frequency 3D image. Study of upgrades to the system, the topology of multiple observation points and the optimized detection algorithm will be future work in this area.

Author Contributions: The research was performed by the authors as follows: Conceptualization, K.Y.; methodology, K.Y. and S.W.; software, K.Y. and S.W.; validation, K.Y. and S.Y.; formal analysis, S.W.; investigation, K.Y. and G.F.; resources, G.F.; data curation, K.Y. and S.Y.; writing—original draft preparation, K.Y.; writing—review and editing, S.W.; visualization, K.Y.; supervision, G.F.; project administration, S.W.; funding acquisition, G.F. All authors have read and agreed to the published version of the manuscript.

Funding: This research work was supported by the National Science Foundation of China under Grant 61971397 and 61501424, the National Key R&D Program of China under Grant 2018YFC0810202. The authors wish to express their gratitude to the editor and the anonymous reviewers.

Institutional Review Board Statement: Not applicable.

Informed Consent Statement: Not applicable

Conflicts of Interest: The authors declare no conflict of interest.

References

1. Yilmaz, B.; Ozdemir, C. A radar sensor design and prototype for through-the-wall imaging radar applications. In Proceedings of the Radar Methods & Systems Workshop (IEEE), Kiev, Ukraine, 27–28 September 2016; pp. 60–63. [\[CrossRef\]](#)
2. Wang, X.; Li, G.; Liu, Y.; Amin, M.G. Two-level block matching pursuit for polarimetric through-wall radar imaging. *IEEE Trans. Geosci. Remote Sens.* **2018**, *56*, 1533–1545. [\[CrossRef\]](#)
3. Yang, S.; Qin, H.; Liang, X.; Gulliver, T.A. Clutter Elimination and Harmonic Suppression of Non-Stationary Life Signs for Long-Range and Through-Wall Human Subject Detection Using Spectral Kurtosis Analysis (SKA)-Based Windowed Fourier Transform (WFT) Method. *Appl. Sci.* **2019**, *9*, 355. [\[CrossRef\]](#)
4. Costanzo, S. Software-Defined Doppler Radar Sensor for Human Breathing Detection. *Sensors* **2019**, *19*, 3085. [\[CrossRef\]](#) [\[PubMed\]](#)
5. Sakamoto, T.; Imasaka, R.; Taki, H.; Sato, T.; Yoshioka, M.; Inoue, K.; Fukuda, T.; Sakai, H. Accurate heartbeat monitoring using ultra-wideband radar. *IEICE Electron. Expr.* **2015**, *12*, 20141197. [\[CrossRef\]](#)
6. Liu, X.; Zhang, J.; Guo, R.; Yang, G.; Ye, S.; Wu, S.; Fang, G. A novel interferometry positioning and tracking method with short baseline for UWB through-the-wall radar system. In Proceedings of the 17th International Conference on Ground Penetrating Radar (GPR), Rapperswil, Switzerland, 18–21 June 2018; pp. 1–4. [\[CrossRef\]](#)
7. Shikhsarmast, F.M.; Lyu, T.; Liang, X.; Zhang, H.; Gulliver, T.A. Random-Noise Denoising and Clutter Elimination of Human Respiration Movements Based on an Improved Time Window Selection Algorithm Using Wavelet Transform. *Sensors* **2019**, *19*, 95. [\[CrossRef\]](#)
8. Yan, J.; Hong, H.; Zhao, H.; Li, Y.; Gu, C.; Zhu, X. Through-Wall Multiple Targets Vital Signs Tracking Based on VMD Algorithm. *Sensors* **2016**, *16*, 1293. [\[CrossRef\]](#)
9. Ding, Y.; Sun, Y.; Zhang, J.; Wang, L. Multiperspective target tracking approach for doppler through-wall radar. *IEEE Geosci. Remote. Sens. Lett.* **2018**, *15*, 1020–1024. [\[CrossRef\]](#)
10. Xia, Z.; Fang, G.; Ye, S.; Zhang, Q.; Chen, C.; Yin, H. A novel handheld pseudo random coded UWB radar for human sensing applications. *IEICE Electron. Expr.* **2014**, *11*, 20140981. [\[CrossRef\]](#)
11. Ash, M.; Ritchie, M.; Chetty, K. On the application of digital moving target indication techniques to short-range FMCW radar data. *IEEE Sens. J.* **2018**, *18*, 4167–4175. [\[CrossRef\]](#)
12. Tantiparimongkol, L.; Phasukkit, P. IR-UWB Pulse Generation Using FPGA Scheme for through Obstacle Human Detection. *Sensors* **2020**, *20*, 3750. [\[CrossRef\]](#)
13. Rittiplang, A.; Phasukkit, P.; Orankitanun, T. Optimal Central Frequency for Non-Contact Vital Sign Detection Using Monocycle UWB Radar. *Sensors* **2020**, *20*, 2916. [\[CrossRef\]](#)
14. Ahmad, F.; Zhang, Y.; Amin, M.G. Three-dimensional wideband beamforming for imaging through a single wall. *IEEE Geosci. Remote. Sens. Lett.* **2008**, *5*, 176–179. [\[CrossRef\]](#)
15. Xu, Y.; Wu, S.; Shao, J.; Chen, J.; Fang, G. Life detection and location by MIMO Ultra wideband radar. In Proceedings of the 14th International Conference on Ground Penetrating Radar (GPR), Shanghai, China, 4–8 June 2012; pp. 80–84. [\[CrossRef\]](#)
16. Liu, J.; Kong, L.; Yang, X.; Liu, Q.H. First-order multipath ghosts' characteristics and suppression in MIMO through-wall imaging. *IEEE Geosci. Remote. Sens. Lett.* **2017**, *13*, 1315–1319. [\[CrossRef\]](#)
17. Rittiplang, A.; Phasukkit, P. 1-Tx/5-Rx Through-Wall UWB Switched-Antenna-Array Radar for Detecting Stationary Humans. *Sensors* **2020**, *20*, 6828. [\[CrossRef\]](#) [\[PubMed\]](#)

18. Liang, F.; Qi, F.; An, Q.; Lv, H.; Chen, F.; Li, Z.; Wang, J. Detection of Multiple Stationary Humans Using UWB MIMO Radar. *Sensors* **2016**, *16*, 1922. [[CrossRef](#)]
19. Geng, Z. Evolution of netted radar systems. *IEEE Access* **2020**, *8*, 124961–124977. [[CrossRef](#)]
20. Jia, Y.; Guo, Y.; Yan, C.; Sheng, H.; Zhong, X. Detection and localization for multiple stationary human targets based on cross-correlation of dual-station SFCW radars. *Remote Sens.* **2019**, *11*, 1428. [[CrossRef](#)]
21. Hunt, A.R. Image formation through walls using a distributed radar sensor array. In Proceedings of the 32nd Applied Imagery Pattern Recognition Workshop, Washington, DC, USA, 15–17 October 2003; pp. 232–237. [[CrossRef](#)]
22. Debes, C.; Amin, M.G.; Zoubir, A.M. Target detection in single- and multiple-view through-the-wall radar imaging. *IEEE Trans. Geosci. Remote Sens.* **2009**, *47*, 1349–1361. [[CrossRef](#)]
23. Sachs, J.; Ley, S.; Just, T.; Chamaani, S.; Helbig, M. Differential Ultra-Wideband Microwave Imaging: Principle Application Challenges. *Sensors* **2018**, *18*, 2136. [[CrossRef](#)]
24. Galajda, P.; Pecovsky, M.; Sokol, M.; Kmec, M.; Kocur, D. Recent Advances in ASIC Development for Enhanced Performance M-Sequence UWB Systems. *Sensors* **2020**, *20*, 4812. [[CrossRef](#)]
25. Xia, Z.; Zhang, Q.; Ye, S.; Wang, Y.; Chen, C.; Yin, H.; Fang, G. A novel low-frequency coded ground penetrating radar for deep detection. *IEICE Electron. Expr.* **2015**, *12*, 20150200. [[CrossRef](#)]
26. Golay, M.J.E. Complementary series. *IEEE Trans. Inf. Theory* **1961**, *7*, 82–87. [[CrossRef](#)]
27. Liu, X.; Yan, K.; Chen, Z.; Li, C.; Zhang, J.; Ye, S.; Fang, G. A m-sequence UWB radar system design and contrast test with an impulse radar. In Proceedings of the 17th International Conference on Ground Penetrating Radar (GPR), Rapperswil, Switzerland, 18–21 June 2018; pp. 1–4. [[CrossRef](#)]
28. Texas Instruments. Time Synchronization over the Air. Available online: http://software-dl.ti.com/simplelink/esd/simplelink_cc13x0_sdk/3.20.00.23/exports/docs/proprietary-rf/proprietary-rf-users-guide/proprietary-rf/time-synchronization.html (accessed on 6 June 2020).
29. Novoselov, S.; Donskov, O. Distributed local positioning system using DWM1000 location chip. In Proceedings of the 4th International Scientific-Practical Conference Problems of Infocommunications, Science and Technology (PIC S&T), Kharkov, Ukraine, 10–13 October 2017; pp. 489–492. [[CrossRef](#)]
30. Gu, Y.; Yang, B. Clock compensation two-way ranging (CC-TWR) based on ultra-wideband communication. In Proceedings of the 8th International Conference on Instrumentation & Measurement, Computer, Communication and Control (IMCCC), Harbin, China, 19–21 July 2018; pp. 1145–1150. [[CrossRef](#)]
31. Zhang, H.; Zhang, Z.; Gao, N.; Xiao, Y.; Meng, Z.; Li, Z. Cost-Effective Wearable Indoor Localization and Motion Analysis via the Integration of UWB and IMU. *Sensors* **2020**, *20*, 344. [[CrossRef](#)] [[PubMed](#)]
32. Sang, C.L.; Steinhagen, B.; Homburg, J.D.; Adams, M.; Hesse, M.; Rückert, U. Identification of NLOS and Multi-Path Conditions in UWB Localization Using Machine Learning Methods. *Appl. Sci.* **2020**, *10*, 3980. [[CrossRef](#)]
33. Liu, X.; Yan, K.; Yang, G.; Ye, S.; Fang, G. Improved vital signal extraction algorithm for through the wall radar. *Electron. Lett.* **2019**, *56*, 89–91. [[CrossRef](#)]